Modulator-Controlled Synthesis of Microporous STA-26, an Interpenetrated 8,3-Connected Zirconium MOF with the *the-i* Topology, and its Reversible Lattice Shift

Alice M. Bumstead,[1] David B. Cordes,[1] Daniel M. Dawson,[1], Kristina K. Chakarova,[2] Mihail Y. Mihaylov,[2] Claire L. Hobday,[3] Tina Düren,[3] Konstantin I. Hadjiivanov,[2] Alexandra M. Z. Slawin,[1] Sharon. E. Ashbrook,[1] Ram R. R. Prasad*[,1] and Paul A. Wright*[,1]

[1] EaStCHEM School of Chemistry, University of St Andrews, Purdie Building, North Haugh, St Andrews KY16 9ST, United Kingdom.

[2] Institute of General and Inorganic Chemistry, Bulgarian Academy of Sciences, Sofia 1113, Bulgaria.

[3]Centre for Advanced Separations Engineering, Department of Chemical Engineering, University of Bath, Bath BA2 7AY, United Kingdom.

*E-mail: rprr@st-andrews.ac.uk; paw2@st-andrews.ac.uk

Abstract A fully interpenetrated 8,3-connected zirconium MOF with the *the-i* topology type, STA-26 (St Andrews porous material-26), has been prepared using the 4,4',4"-(2,4,6-trimethylbenzene-1,3,5-triyl)tribenzoate (TMTB) tritopic linker with formic acid as a modulating agent. In the as-prepared form STA-26 possesses *Im*-3*m* symmetry compared with the *Pm*-3*m* symmetry of the non-interpenetrated analogue, NU-1200, prepared using benzoic acid as a modulator. Upon removal of residual solvent there is a shift between the interpenetrating lattices and a resultant symmetry change to *Cmcm* which is fully reversible. This is observed by X-ray diffraction and ^{13}C MAS NMR is also found to be remarkably sensitive to the structural transition. Furthermore, heating STA-26(Zr) in vacuum dehydroxylates the Zr_6 nodes leaving coordinatively unsaturated Zr^{4+} sites, as shown by IR

spectroscopy using CO and CD_3CN as probe molecules. Nitrogen adsorption at 77 K together with grand canonical Monte Carlo simulations confirms a microporous, fully interpenetrated, structure with pore volume 0.53 $cm^3\ g^{-1}$ while CO_2 adsorption at 196 K reaches 300 cm^3 STP g^{-1} at 1 bar. While the pore volume is smaller than that of its non-interpenetrated mesoporous analogue, interpenetration makes the structure more stable to moisture adsorption and introduces shape selectivity in adsorption.

Introduction

The diverse and growing family of porous metal-organic frameworks (MOFs),[1] constructed from metal-based nodes and organic linkers, offers a range of potential applications in adsorption,[2] sensing,[3] catalysis[4] and drug delivery.[5] Among these many materials, the zirconium carboxylates offer some of the most porous and also the most chemically and thermally stable examples.[6] Many of these are based on the Zr_6O_8 building block, which may adopt 12-, 10-, 8- or 6-fold coordination with di-, tri- or tetracarboxylate groups of linker molecules, to give structures with *fcu, bct, csq* and *spn* topologies.[7] A zirconium carboxylate MOF with the 8,3-connected ***the*** topology type, formed with the 4,4',4"-(2,4,6-trimethylbenzene-1,3,5-triyl)tribenzoate (TMTB) tritopic linker, was recently reported by two groups and assigned the names NU-1200[8] and BUT-12.[9] The structure consists of a primitive cubic arrangement of corner-sharing cages with octahedral geometry, each of which possesses a sodalite-like *(sod)* cage structure (Figure 1). Each 'superoctahedral' cage comprises six Zr_6O_8 clusters linked via tritopic TMTB linkers on the faces of the octahedron, and has an internal free diameter of 1.4 nm. Each Zr_6O_8 cluster is linked to eight others in a square prismatic arrangement. Charge balance in NU-1200 is reportedly achieved by the addition of hydroxyl groups and water molecules to the zirconium clusters, giving an overall

framework formula $Zr_6(\mu_3O)_4(\mu_3OH)_4(OH)_4(OH_2)_4(C_{30}H_{24}O_6)_{8/3}$.[10,11] Between these 'superoctahedral' cages is a mesoporous pore space, accessible via 2 nm windows, which is of great interest as a potential host for adsorbates or for species that are catalytically active for the transformation of large molecules.

The reported syntheses of NU-1200 and BUT-12 are similar, but make use of different carboxylic acids as modulators. Modulators have been observed to have a strong effect on MOF crystallisation, controlling particle size and morphology, the density of 'missing linker' defects and even the phase that is formed.[12] Even though the length and flexibility of linkers[13-15] and the influence of solvents[16,17] on regulating the degree of interpenetration has been observed previously, the role of modulators in governing the synthesis of interpenetrated MOFs has not, to the best of our knowledge.

Here we report the role of modulators in controlling the interpenetration in a zirconium MOFs with the *the* framework topology, and its hafnium analogue. Interpenetration, in which identical lattices have grown one within the other, is observed in many MOFs where their geometry and dimensions allow, and where interactions between the interpenetrating lattices are favourable.[18] The zirconium amino-terephthalate MOF UiO-66(NH_2) and related structural forms with longer ditopic linkers, for example, have been shown to form interpenetrated frameworks, the crystallinity of which can be enhanced by the use of modulators.[14]

We designate the interpenetrated Zr-MOF framework STA-26 (St Andrews porous material-26) and have characterised its structure, porosity and properties fully. Complementary single crystal X-ray diffraction and N_2 and CO_2 adsorption (together with molecular simulation of the adsorption) show it is microporous rather than mesoporous; powder diffraction and solid state NMR reveal details of a relative lattice shift upon post-synthetic treatment that modifies

the window size; IR spectroscopy is used to investigate its adsorption sites; and interpenetration imparts enhanced stability to moisture. Furthermore, we have prepared the hafnium-version of this material, in the knowledge that Hf has similar chemistry in MOF frameworks but that Hf-MOFs can possess properties significantly different from those of their Zr-analogues.[19]

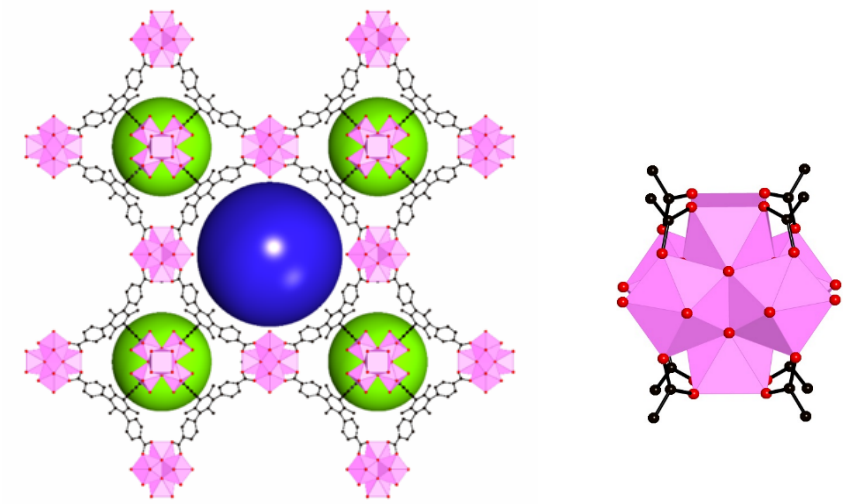

Figure 1 (Left) Polyhedral and ball-stick representation of the structure of NU-1200, which has the *the* topology type. The mesoporous cages of NU-1200 are shown by the blue sphere while the space within the sodalite-like cages are shown by the green spheres. (Right) The 8-connected Zr_6 cluster of NU-1200. Hydrogen atoms are omitted for clarity.

Results and Discussion

A modified NU-1200 synthesis, based on a literature procedure which used benzoic acid as a modulator, gave a material with a PXRD pattern that matched that simulated from the published, non-interpenetrated, structure of NU-1200 in *Pm*-3*m*, with unit cell parameter of 28.300 Å (Figures S1 and S2).[8] Initial synthesis attempts using formic acid as a modulator,

similar to those reported for the synthesis of BUT-12[9] and with a DMF:formic acid molar ratio of 1:2 (8 ml: 8 ml) gave crystalline solids with a PXRD pattern which could be indexed to a primitive cell with a very similar unit cell parameter to NU-1200 (28.169 Å) but with strongly different diffraction intensities (Figure 2). Solution-state ^{1}H NMR spectra of the dissolved Zr-MOF showed peaks from the TMTB ligand and also from residual DMF. It was possible to pick out single crystals from these preparations that were sufficiently large for laboratory single crystal diffraction (Figure S3).

After screening different DMF:formic acid molar ratios (Figure S4), it was found that a 1:1.2 molar ratio of DMF:formic acid (10 ml: 6 ml) gave a microcrystalline material comprising cubic crystals *ca*. 1-2 μm in dimension (Figure S5). In this case the PXRD pattern (Figure 2, right) could be indexed as body-centred cubic, with a similar unit cell to those preparations described above, and this Zr-MOF was designated STA-26(Zr) (STA = St Andrews porous material). Notably, in the absence of formic acid modulator, no crystalline solid forms, whereas adding smaller amounts of formic acid (DMF:formic acid molar ratio 5.8:1) or higher amounts of formic acid (DMF:formic acid 1:2) gives solids for which the PXRD shows considerable intensity in peaks that violate the I-centring that is clearly demonstrated by pure STA-26(Zr) (Figure S4).

A hafnium version, STA-26(Hf), was also prepared with a PXRD pattern that could be indexed to a body-centred cell, unit cell parameter 28.317 Å (Figure 2).

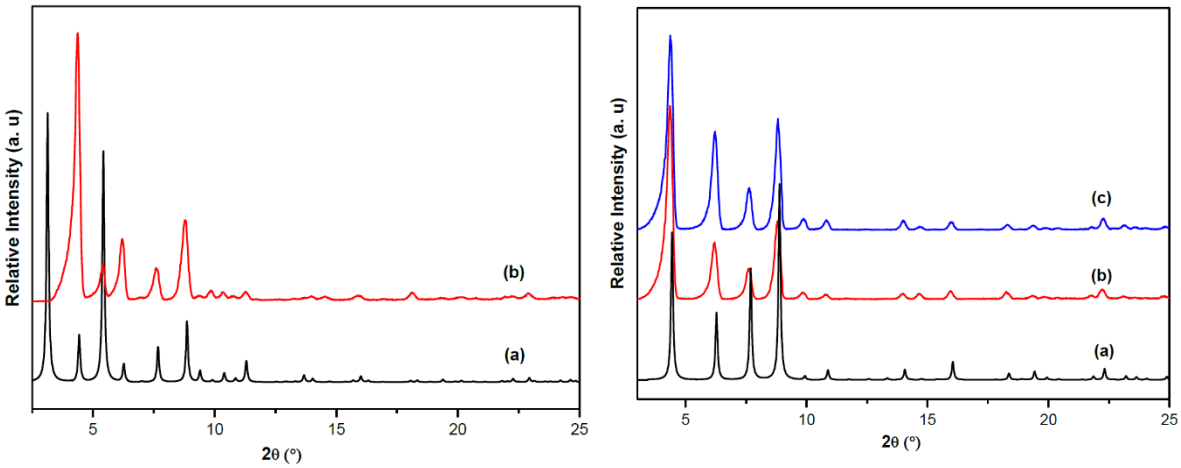

Figure 2 (Left) (a) Simulated PXRD pattern of NU-1200(Zr) compared with (b) that of as-synthesised STA-26(Zr) prepared with DMF:formic acid molar ratio 1:2. (Right) (a) Simulated PXRD of STA-26(Zr) compared with those of (b) as-synthesised STA-26(Zr) and (c) as-synthesised STA-26(Hf) (each with a 1:1.2 molar ratio of DMF:formic acid).

SCXRD of a selected crystal of the product from the preparation with a DMF:formic acid molar ratio of 1:2 revealed a structure with cubic symmetry, space group *Im*−3*m* (Table 1 and Figure 3, left). The PXRD pattern simulated from this structure solution is a close fit to that observed for both Zr and Hf versions of STA-26 (Figure 2, right), with the small differences in intensity in the low angle peaks attributable to the presence of disordered solvent remaining in the pores. The pattern is very different from that of the non-interpenetrated NU-1200, compared directly in Figure 3 (right). This indicates that the I-centred STA-26(Zr) possesses an interpenetrated structure, with two identical lattices of the *the* topology, each with a structure similar to that of the NU-1200 framework, displaced by a lattice vector [½,½,½]. The TMTB linkers exhibit 90° rotation of the benzoate groups with respect to the central mesitylene core that is characteristic of this linker, and which results in crystallisation of the *the* 8,3-topology. In STA-26, the sodalite-like cages of one of the interpenetrating frameworks now occupy the mesoporous cavities of the other.

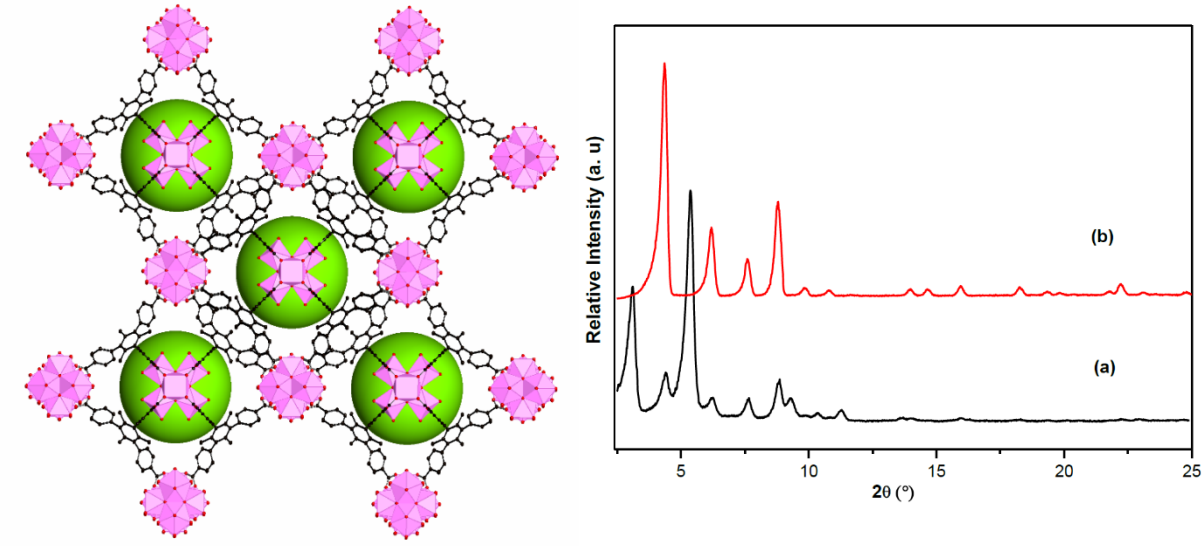

Figure 3. (Left) Structure of STA-26(Zr) with *Im*-3*m* symmetry. It is an interpenetrated analogue of NU-1200, shown in Figure 1. (Right) PXRD patterns of as-synthesised (a) NU-1200(Zr) and (b) STA-26(Zr)

The linkers of the interpenetrated networks at their closest point display a distance of 5.16 Å between the centres of C atoms of the adjacent benzene rings. Pore openings with a width of 4.80 Å (once van der Waals radii are taken into account) lead to octahedral cages of internal diameter 14 Å (similar to those of NU-1200). To the best of our knowledge, an interpenetrated Zr-MOF with 8-connected Zr_6O_8 clusters has not been reported, although it has been shown that by fine tuning the planarity of triangular tetrazolate-based linkers used in the synthesis of copper benzene- or triazine-centered tetrazolates the *the* and *the-i* topology can be achieved for 8,3-connected frameworks.[15]

Since both NU-1200 and STA-26 have the same overall composition (metal clusters and linkers), the difference in structure must arise from the use of different modulators in the solvothermal preparations. As the formic, benzoic and 2-fluorobenzoic acids have very similar *p*Ka values (3.8, 4.2 and 3.8)[20] this originates from the different steric effects when attached to the Zr_6 clusters during crystal growth. It should be noted that no formate species

were observed in the digested STA-26 by solution-phase NMR (Figure S6) although benzoic acid was observed in digested NU-1200 (Figure S7).

Although the bulk sample from which the single crystal was taken showed reflections in the powder pattern that violate body centring, prolonged immersion of the bulk '1:2' sample in DMF post-synthesis, followed by drying in air, gave a bulk sample with a body-centred powder pattern similar to that observed for the small crystal '1:1.2' preparation. This suggested that both samples had the same interpenetrated structure, and that the additional peaks derived from a reversible symmetry change related to residual DMF content (Fig. S8).

Table. 1 Crystallographic data for STA-26(Zr) and STA-26(Zr)-*C*

Label	STA-26(Zr)	STA-26(Zr)-*C*
Formula	$C_{40}H_{36}O_{16}Zr_3$	$C_{40}H_{36}O_{16}Zr_3$
Formula weight/g mol^{-1}	1046.35	1046.35
Temperature/K	173	173
Crystal system	Cubic	Orthorhombic
Space group	$Im\bar{3}m$	*Cmcm*
a/Å	28.16930 (14)	40.3620 (8)
b/Å	-	39.8384 (8)
c/Å	-	27.9686 (5)
V/Å	22352.6(3)	44972.3(15)
Z	12	24
ϱ(calcd) g cm-3	0.933	0.927
Radiation type	Cu Kα	Cu Kα
μ mm-1	3.725	3.703
F(000)	6288	12576
Rint	0.1007	0.1908
GOF	1.069	1.426
Final R1 values [I >2σ(I)][a]	0.0618	0.1309
Final wR2 values (all data)[b]	0.1977	0.3662

Structural changes upon activation for adsorption measurements

In order to optimise the accessible pore volume of STA-26(Zr), samples were repeatedly washed with acetone and subsequently dried at 80 °C prior to measurement of N_2 adsorption at 77 K. Under these conditions, the PXRD pattern displays additional reflections that violate the *I*-centring. Subsequent immersion in DMF and drying gave a sample with the original *I*-centred pattern (Figure 4). STA-26(Hf) showed similar behaviour when treated under these conditions (Figure S9). Further, VT-PXRD of STA-26(Zr) shows a loss of *I*-centring upon heating, which was not reversed on cooling (Figure 5). Taken together, these observations suggest that traces of residual DMF solvent keep the interpenetrated lattices apart, whereas their removal results in a structural change that was reversible by re-introduction of DMF.

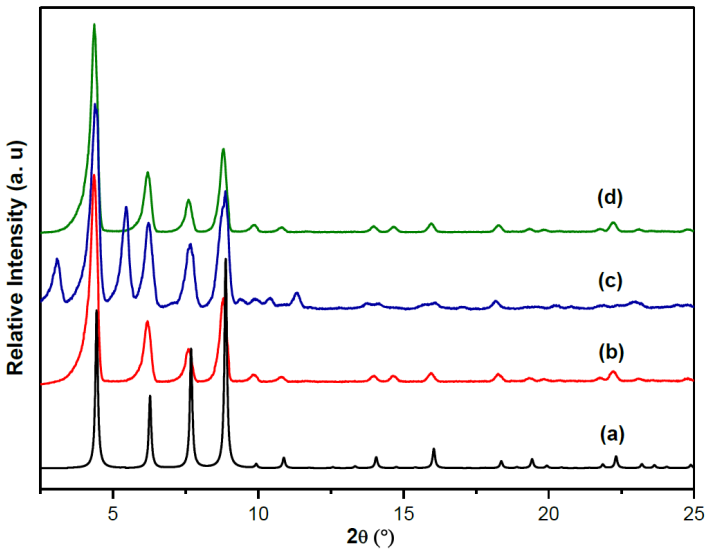

Figure 4 Comparison of (a) the simulated PXRD pattern for STA-26(Zr) with those of (b) as-synthesised STA-26(Zr) (1:1.2 prep.), (c) STA-26(Zr) after 1 week in acetone with solvent exchange every 24 h, followed by drying, (d) after immersion in DMF and drying.

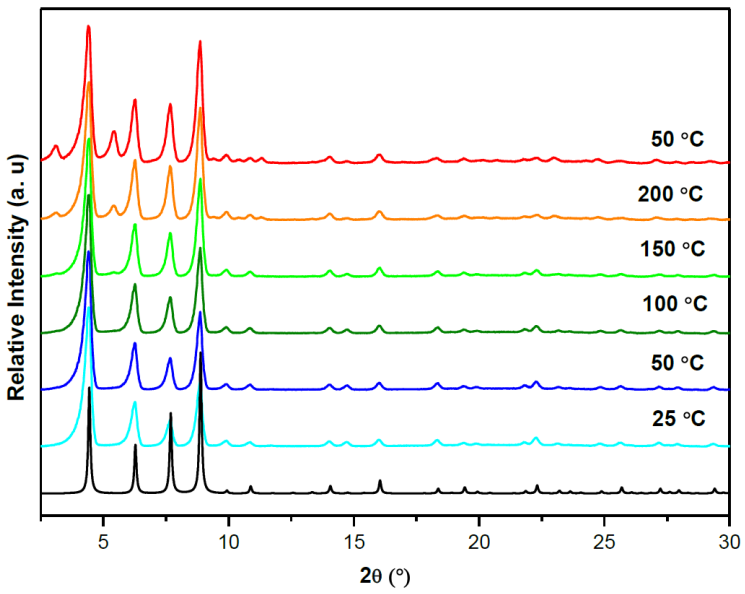

Figure 5 VT-PXRD of as-synthesised STA-26(Zr) heated from 25 °C to 200 °C and then cooled to 50 °C, compared with simulated pattern for as-synthesised STA-26(Zr), the black curve.

To investigate this further, SCXRD was performed on a single crystal of as-synthesised STA-26(Zr) that had been kept in acetone for a week with the solvent replaced every 24 h and subsequently dried at 80 °C. The structure was solved in the orthorhombic *Cmcm* space group, and is here referred to as STA-26(Zr)-*C* (See Table 1 and the cif file in the ESI for crystallographic details). There has been a relative movement of one lattice with respect to the other, changing the distance between the TMTB linkers and the Zr_6O_8 clusters of the two frameworks (Figure 6). Whereas in body-centred STA-26(Zr) the distance between the central phenyl ring of the TMTB of adjacent linkers is the same in every case (4.74 Å), in STA-26(Zr)-C there are three different distances, 3.571 Å, 4.74 Å and 7.41 Å. Consequently, STA-26(Zr)-*C* possesses three different pore openings with free diameters 3.57 Å, 4.43 Å and 5.24 Å leading to cages of unchanged internal diameter (14 Å). This relative movement of the interpenetrating frameworks changes the overall symmetry of the structure, so that instead of

a single crystallographic environment for the linkers in STA-26(Zr), there are now three different sets of linker environments in STA-26(Zr)-*C*.

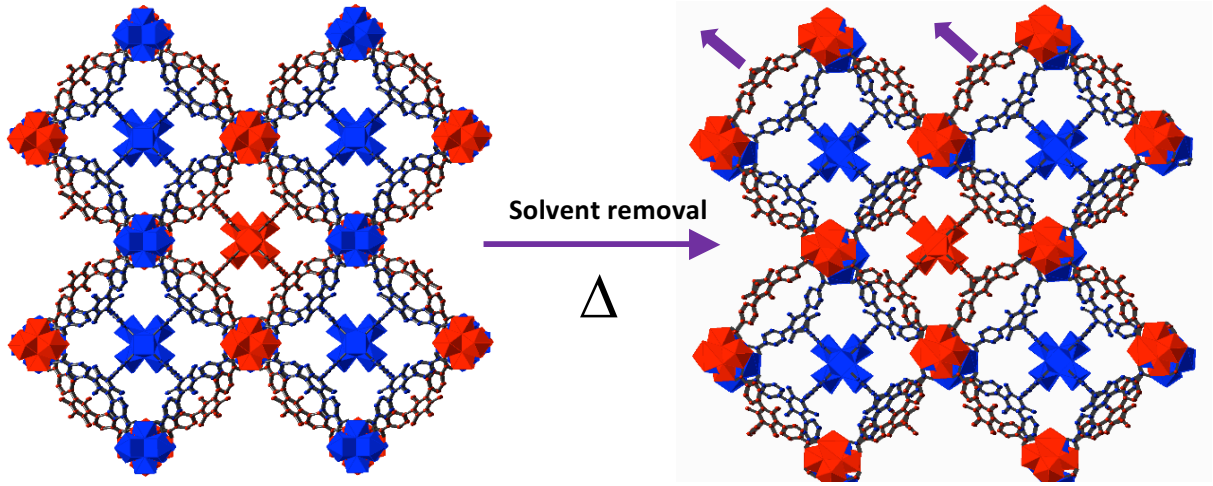

Figure 6 Structural change of (left) STA-26(Zr) (*Im*−3*m*) to (right) STA-26(Zr)-*C* *(Cmcm)* upon removal of residual solvent molecules. The relative direction of lattice movement of one of the interpenetrated lattices (with clusters in red) is denoted by purple arrows.

Owing to its sensitivity to small changes in the local structure, solid-state ^{13}C NMR spectroscopy can be used to follow this structural transition. For body-centred STA-26(Zr), each of the chemically-distinct carbon atoms of the TMTB linker structure gives a single resonance, as expected from the symmetry (Figures 7 and S10, and S11 for the Hf-form). Notably, the spectrum is similar to that observed for the non-interpenetrated NU-1200 (Figure S12), in which the ligands are all crystallographically equivalent, but with small changes in chemical shift. In the ^{13}C CP MAS NMR spectrum of STA-26(Zr)-*C* prepared by solvent removal, each of the signals shows splittings that indicate the presence of distinct crystallographic environments, due to the relative movement of the frameworks. As an example, whereas there is only one crystallographically distinct CH_3 in the *I*-centred structure, there are eight in the C-centred structure, giving rise to the observed splitting in the resonance at 16-18 ppm.

When the desolvated structure is reimmersed in DMF, the splittings of the spectral resonances disappear and the spectrum is similar to that of the original STA-26(Zr) (Figure 7). This confirms that the *I*-centred structure is stabilised by the introduction of solvent molecules residing in the pores. If these are removed either by continuous solvent exchange and/or heating, one lattice moves with respect to each other to achieve a lower energy position.

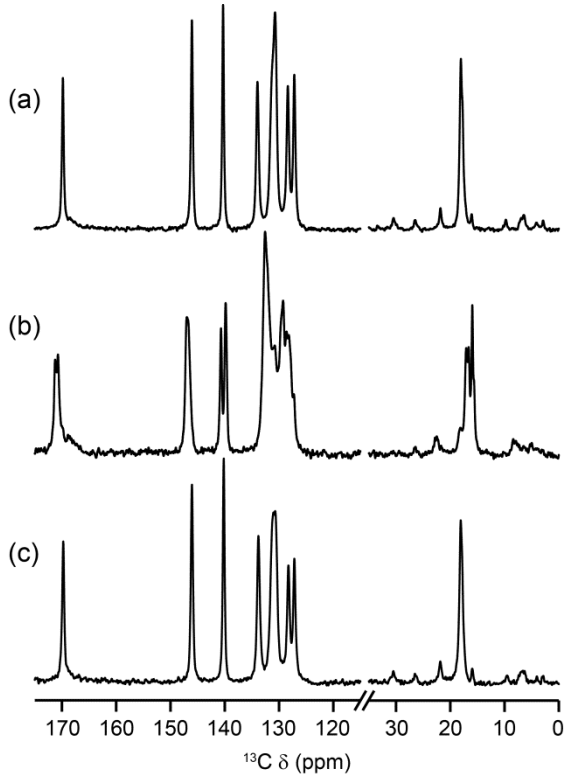

Figure 7 ^{13}C CP MAS NMR spectra of (a) as-synthesised STA-26(Zr), (b) STA-26(Zr)-*C* obtained after prolonged solvent exchange with acetone and (c) after reimmersion in DMF.

It is notable that as-synthesised materials showing PXRD peaks of relatively low intensity violating the *I*-centring also show splittings in the ^{13}C CP MAS NMR spectrum, although these are not as large as when washed and dried at 80 °C (Figure S14). It is likely that this is

a result of intermediate stages of framework movement where the structure contains different levels of DMF.

Furthermore, the effect of immersion of the C-form of STA-26 in other solvent molecules (Figure S13) showed that while DMF caused full return to I symmetry, tetrahydrofuran had no effect while the bulkier N,N-dibutyl- and N,N-diethylformamide strongly reduced the intensities of reflections attributed to the 'off-centring' of the second lattice. This indicates solvent polarity plays a controlling role in this effect.

VT-PXRD of STA-26(Zr)-*C* showed that the lattice-shifted structure is stable and no further symmetry changes occur up to 200 °C (Figure 8). The overall crystallinity of the structure is retained after the experiment and when cooled down to room temperature, and there is now very close agreement between observed solvent-free STA-26(Zr)-*C* and the pattern simulated from the crystal structure.

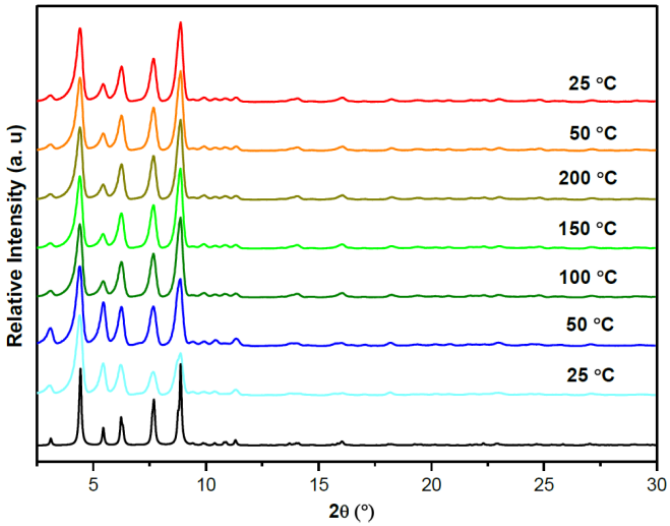

Figure 8. VT-PXRD patterns of STA-26(Zr)-*C* from 25 °C to 200 °C and then cooled down to 50 °C and 25 °C with simulated pattern of STA-26(Zr)-*C*.

TGA of as-prepared samples of STA-26(Zr) (Figure S15) indicates an initial weight loss of 8% corresponding to the removal of adsorbed volatile solvent molecules residing in the pores and another loss of 8% around 150-300 °C, which can be attributed to the dehydroxylation of the Zr_6 clusters and removal of residual DMF. The structure decomposes above 400 °C.

Figure 9 shows the IR spectra of STA-26, as-prepared and evacuated at room temperature. The two strong bands at 1600 and 1406 cm^{-1} are assigned to coordinated carboxylates.[21] The as-prepared sample is characterized by a broad band at 3400 cm^{-1} due to adsorbed water. Evacuation at RT removes this band completely, indicating weak water adsorption. Therefore, the sample treated in this way has few strong adsorption sites such as co-ordinately unsaturated Zr sites associated with missing-linker defects.

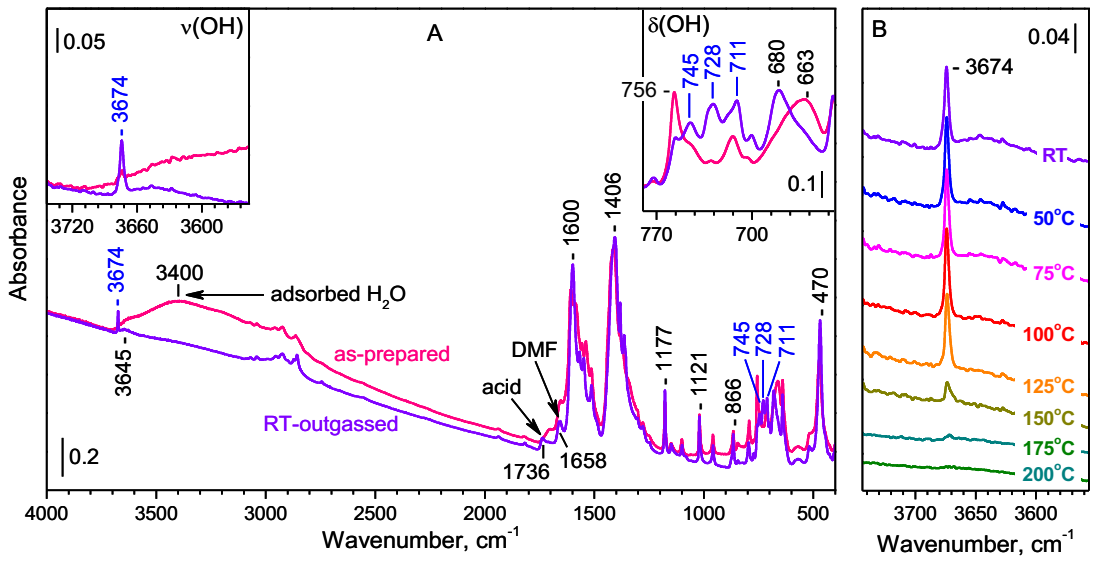

Figure 9. (a) IR spectra of (left) STA-26(Zr) as-prepared (pink) and evacuated at room temperature (violet) and (b) IR spectra showing the dehydroxylation of STA-26(Zr).

Water desorption leads to development of a sharp band in the OH stretch region at 3674 cm^{-1} due to isolated OH groups attached to zirconium oxide clusters.[21-23] For the related Zr MOF

NU-1000, this band was attributed to include vibrations of terminal and bridging OH groups.[23] Surprisingly, three deformation OH bands at 745, 729 and 711 cm^{-1} also appeared, but deuteration of the sample (see Figure S16) produced one OD deformation band. This revealed that the three OH bands are not indicative of heterogeneity of OH groups but rather are a consequence of a spectroscopic effect arising from mixing of OH deformation modes with other MOF vibrations. These OH groups are of low acidity as the water H-bonded to them can be easily removed. A weak and broad feature around 3645 cm^{-1} is probably due to a small fraction of weakly H-bonded hydroxyls OH groups affected by strongly bound adsorbates. Residual DMF (1659 cm^{-1}) and free acid (1736 cm^{-1}) are observed for the room temperature evacuated sample. The DMF is removed upon outgassing at 175 ºC.

The stability of intra-framework hydroxyls was studied upon stepwise heating in vacuum. The dehydroxylation of STA-26(Zr) sample starts at 100 ºC, proceeds gradually with heating, and is completed at 200 ºC (Figure 9). This process was found to be reversible. The dehydroxylation route can be described as condensation of hydroxyl groups: $2OH \rightarrow O^{2-} + H_2O$. This is in accordance with the TGA of STA-26(Zr). The picture is similar to that observed for NU-1200 and is attributed to the loss of water and hydroxyl groups from the Zr_6O_8 clusters.[10,11]

To investigate changes in the internal surface chemistry of STA-26(Zr) upon heating, CO, CD_3CN and CO_2 were used as probe molecules in an extended IR spectroscopic study. The adsorption of probe molecules was examined for both hydroxylated and dehydroxylated forms of STA-26(Zr).

Surface acidity was assessed by adsorption of CO and CD_3CN at cryogenic and ambient temperature, respectively (Figure 10). With the hydroxylated sample both probes reveal the existence of weak Brønsted acidity which is typical of MOF materials.[24,25] Adsorption of CO

leads to development of an OH···CO band at 2149 cm^{-1} (Figure 10A). Simultaneously, a red shift of the OH stretching band of 68 cm^{-1} is detected (note that the largest such shift reported with MOF materials is 90 cm^{-1} [26]). The OH···$NCCD_3$ complexes were detected at 2273 cm^{-1}.

The bands associated with OH···CO and OH···$NCCD_3$ species appeared with strongly reduced intensities on the dehydroxylated sample. However, in this case, bands indicative of the presence of open Zr^{4+} sites were detected (Zr^{4+}···CO at 2170 cm^{-1} and Zr^{4+}···$NCCD_3$ at 2300 cm^{-1}, see Figs. 10B and D, respectively). Note that, as a strong base, CD_3CN can displace water adsorbed on Lewis acid sites and can thus detect some open Zr^{4+} sites that are not visible by CO as a probe. However, it appears that the concentration of such sites is negligible, as indicated by the very weak feature around 2300 cm^{-1} in Figure 10C. These results rule out the existence in our sample of a large fraction of clusters terminated by water ligands only.

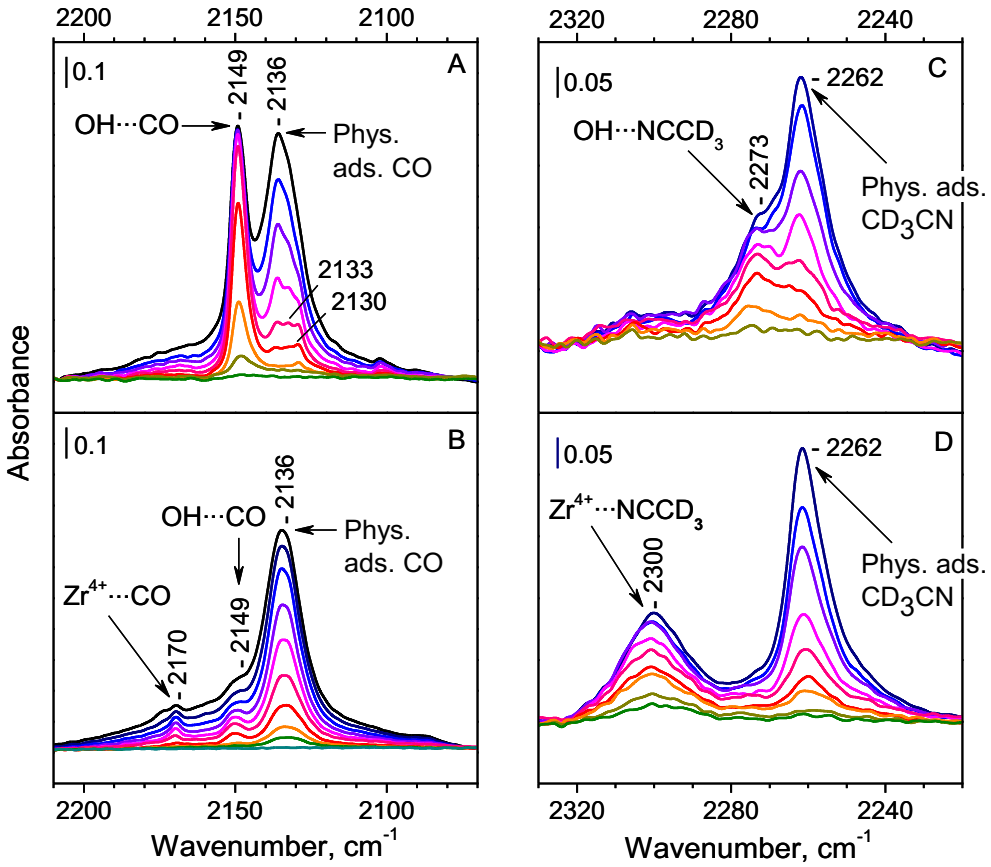

Figure 10. (A, B) IR spectra of CO adsorbed at 100 K and (C, D) CD_3CN adsorbed at room temperature on STA-26(Zr) sample evacuated at room temperature (upper panels) and at 175°C (bottom panels), with spectra from continually increasing doses of the IR probe gases represented in green to blue.

Spectra of adsorbed CO_2 were acquired at room temperature with CO_2 equilibrium pressure varied in the 1 – 50 mbar range. The $\nu_{as}(CO_2)$ bands obtained with the dehydroxylated STA-26(Zr) sample (Figure 11B) are less than one-half the intensity of the hydroxylated material (Figure 11A).This indicates that the OH groups can play an important role as adsorption sites for CO_2. The second derivatives of the spectra (shown in the left insets) reveal that the main band consists of two components. The high frequency component can be related to CO_2 adsorbed on structural OH groups (OH-OCO) because (i) it is hardly observed with the

highly dehydroxylated sample and (ii) it correlates with the shift of the OH stretching band (see the right inset in Figure 11A). The low frequency component can be attributed to weakly and non-specifically adsorbed CO_2.

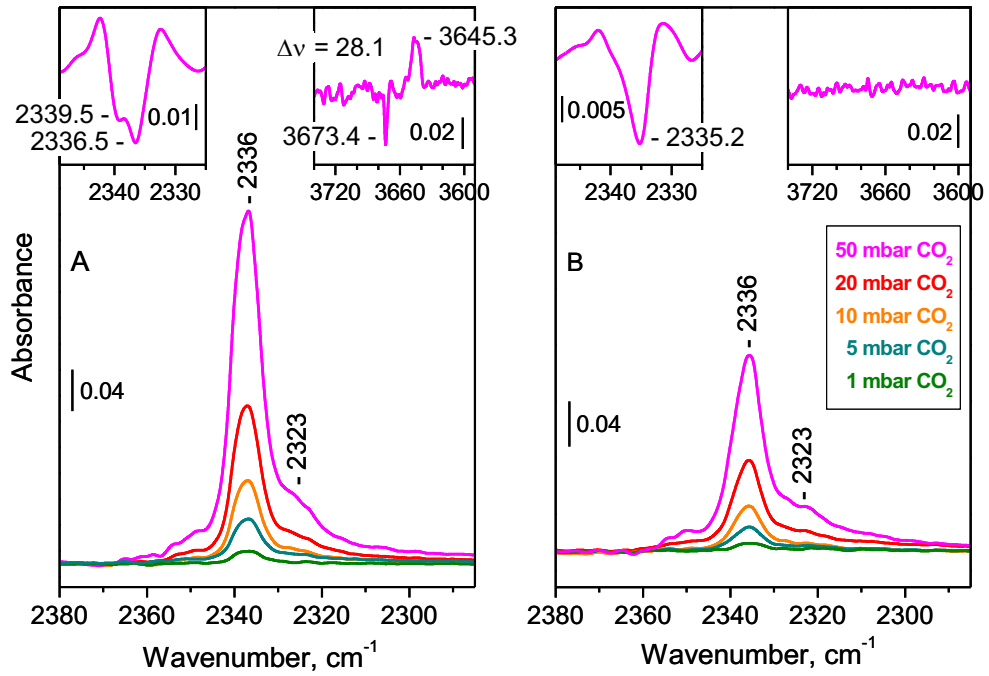

Figure 11. (A) IR spectra of CO_2 adsorption of STA-26(Zr) evacuated at room temperature and (B) at 150 °C.

The pore structure of STA-26 was probed by N_2 and CO_2 adsorption measurements, after an activation protocol that, according to our IR and PXRD studies, dehydroxylates the clusters and results in conversion to the STA-26(Zr)-*C* form. N_2 adsorption at 77 K gives a Type I isotherm typical of a microporous solid (Figure 12, left). This contrasts strongly with that reported for NU-1200[8] and the isotherm measured for the NU-1200 prepared in this work (Figure S17), both of which show a Type IV isotherm typical of a mesoporous structure.

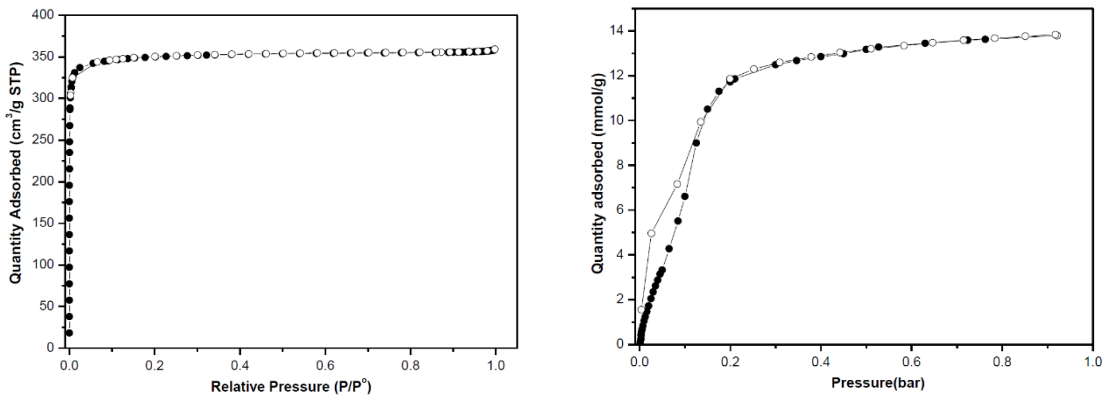

Figure 12. (Left) N_2 adsorption isotherm at 77 K and (right) CO_2 adsorption isotherm at 196 K measured for STA-26(Zr) activated at 150 °C for 16 h (closed symbols), with desorption (open symbols).

Simulated nitrogen adsorption isotherms in STA-26(Zr)-*C* and NU-1200 (Figure 13) show reasonable agreement with the experimentally measured isotherms, although the total pore volume is higher than that measured, presumably because not all the pore space is accessible, or there is some loss of structure. For STA-26, around 75% of the calculated value is observed. Note that the lattice shift (*I* to *C* transition) has only a very minor effect on the simulated adsorption isotherm.

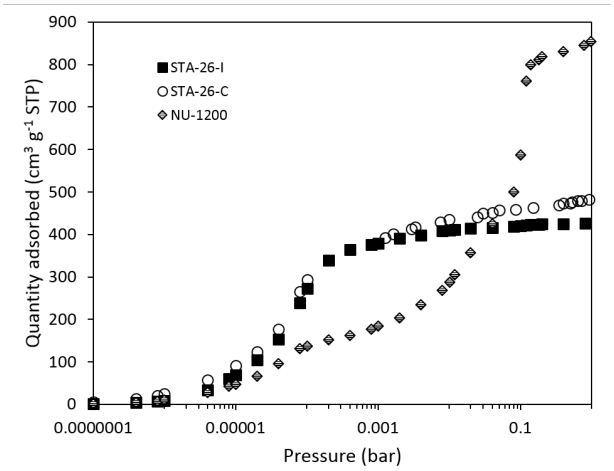

Figure 13. Simulated N_2 adsorption isotherms for STA-26(Zr)-*I*, STA-26(Zr)-*C* and NU-1200 at 77 K.

These results emphasise that, while non-interpenetrated NU-1200 is mesoporous, with pore volume deriving both from the space within the *sod* cages and the mesoporous space between them, in STA-26 the mesoporous cavities of one *the* framework are occupied by *sod* cages of the other, giving a microporous material. This confirms our interpretation of the single crystal XRD, which might without the N_2 adsorption data also be interpreted as a partially interpenetrated structure, with each of the lattices having the same fractional occupancy. Such a structure would possess some mesoporosity and so show an inflexion in the N_2 adsorption isotherm.

CO_2 adsorption measured at 196 K approaches 300 cm^3 STP g^{-1}, 1 bar (Figure 12 right), and at 298 K reaches 160 cm^3 STP g^{-1} at 10 bar (Figure S18), in each case showing an inflection at around 80 cm^3 STP g^{-1}. GCMC simulations of the adsorption isotherms of CO2 on STA-26(Zr) and NU-1200 at 196 K are shown in Figure S19. Comparison with the observed isotherm confirms that STA-26 is fully interpenetrated and microporous. The simulations also yield detailed information about the guest-framework interaction and the location of the guest molecules. Figure 14 shows histograms of the simulated CO_2 / MOF interaction energies at 1 bar. While NU-1200 has some low energy sites (i.e. strong interaction sites) mainly around the Zr-nodes of the framework (Figure 14d), the adsorption behaviour is dominated by weak adsorption sites (interaction energies ~ −2 kJ mol^{-1}) in the centre of the octahedral pores. In STA-26(Zr)-*C* the Zr-clusters act as strong adsorption sites, and furthermore interpenetration in STA-26(Zr)-C results in smaller pore sizes and stronger adsorption sites (Figure 13a and c). Simulated adsorption surfaces of CO_2 at 0.01 bar on STA-26(Zr)-*I* and *C* show that the lattice shift gives rise to an additional adsorption site in the void between phenyl groups of neighbouring interpenetrating nets (Figure S20).

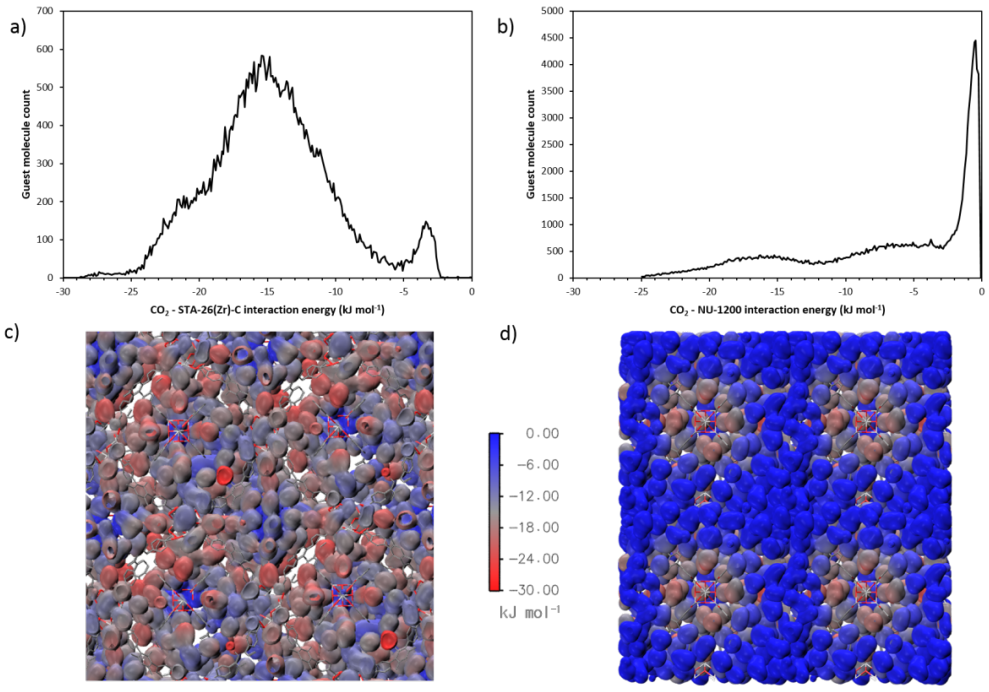

Figure 14. Energy density distributions of CO_2/MOF interactions in *(a)* STA-26*(Zr)-C* and (b) NU-1200 at 196 K and 1 bar. (c) and (d) Surface plots of the CO_2/MOF interaction energy, where blue = 0 kJ mol^{-1} and red = -30 kJ mol^{-1}.

To demonstrate the difference in window size between microporous STA-26(Zr) and mesoporous NU-1200, dye uptake and catalytic behaviour of the MOF were also studied. Following the previous dye uptake studies performed by Lin et al.,[27] NU-1200 and STA-26 were kept in ethanolic solutions of Fuchsin basic dye for 10 h, followed by subsequent filtration and multiple washes with ethanol. Mesoporous pore openings enable NU-1200 to achieve higher levels of dye uptake in comparison with STA-26(Zr), as clearly indicated by the difference in intensity of colour (Figure 15).

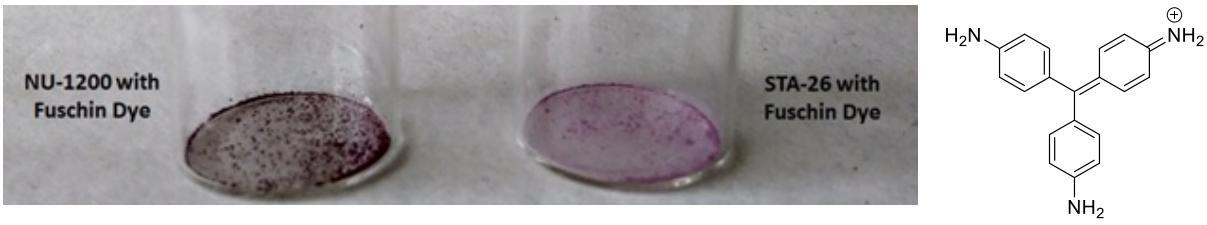

Figure 15. NU-1200 and STA-26(Zr) after exposure to a solution of Fuchsin basic dye (right).

Furthermore, in the Lewis acid-catalysed condensation of 4'-fluoroacetophenone and benzylamine (Scheme S1), STA-26(Zr) gave only 28% conversion towards the imine, in comparison with 51% for the NU-1200 (Figure S21). As both MOFs possess similar Zr_6O_8 clusters, the higher conversion rates of NU-1200 are attributed to the free movement of the large reactant and product molecules within its mesopores, while the lower observed conversion over microporous STA-26 could result from surface catalysis.

Thermal and water stability of MOFs are two major concerns that limit their application. While the thermal stability has been steadily improved[7, 28] the water instability of MOFs remains a significant limitation. One cause of instability, giving rise to extremely low surface areas after activation from water, is the high capillary forces acting on the walls of pores containing water.[29] Consequently, MOFs are best activated after being kept in low boiling point solvents or in supercritical CO_2.[30] As interpenetration has been reported to increase the overall stability of MOFs,[13] we tested the water stability of STA-26(Zr). Following the protocol by Farha et al., as-prepared STA-26(Zr) was kept in water for 48 h and subsequently activated at 100 °C.[31] PXRD showed peaks corresponding to change in symmetry and can be indexed to STA-26(Zr) showing the I to C symmetry change. The overall crystallinity of the MOF was well-preserved under these conditions (Figure 16). By contrast, when NU-1200 was kept in water and activated under similar conditions, some broadening of reflections occurred. Furthermore, at 77 K, the N_2 adsorption isotherm of NU-1200 activated directly from water showed significantly lower porosity, while STA-26(Zr) retained its porous nature. This indicates that the interpenetrated geometry of STA-26 enhances its stability to water.

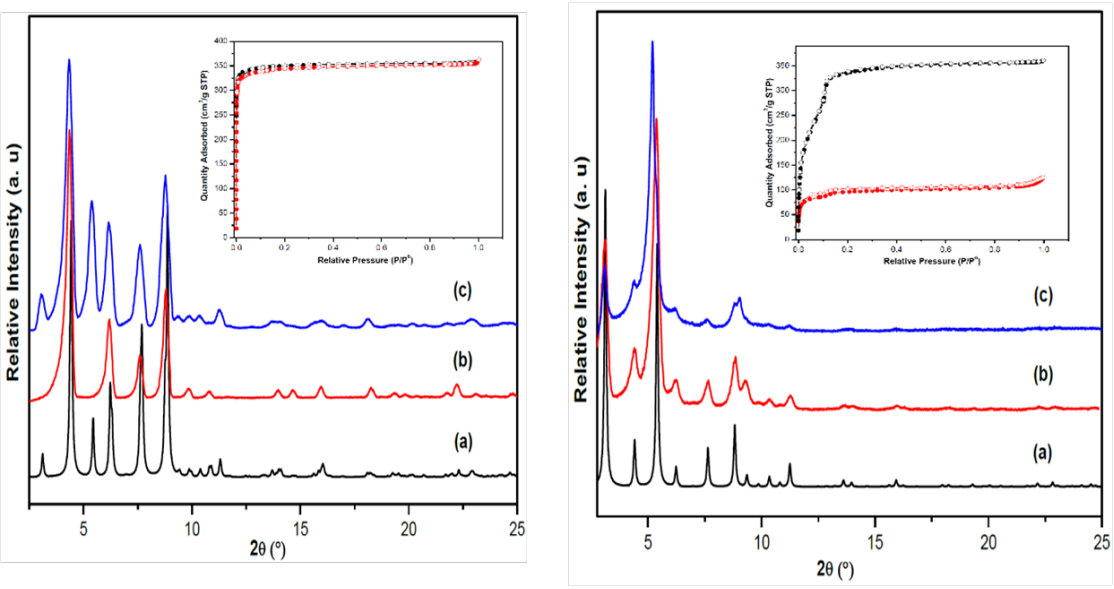

Figure 16. Left, (a) Simulated PXRD pattern for STA-26(Zr)-*C*, (b) as-prepared STA-26(Zr), (c) STA-26(Zr) after 48 h water stability test and direct activation from water. Inset: N_2 isotherm of STA-26(Zr) activated at 150 °C after solvent exchange with acetone (black) and directly activated from water (red). Right, (a) simulated PXRD pattern for NU-1200, (b) as-prepared NU-1200, (c) NU-1200 after water stability test and direct activation from water. Inset: N_2 isotherm of NU-1200 activated at 150 °C after solvent exchange with acetone (black) and directly activated from water (red).

Conclusions

A route has been devised to a fully interpenetrated version of the Zr-based MOF, NU-1200, which we denote STA-26(Zr). The Hf-analogue of STA-26 has also been prepared. As in NU-1200, the TMTB linker in STA-26 shows the characteristic geometry, where the presence of the methyl groups on the central benzene ring of the linker results in rotation of the benzoate groups and consequently favours the *the* topology type with eight-connected Zr_6O_8 clusters. In the STA-26 structure, two lattices with the *the* topology type interpenetrate.

Whether the interpenetrated or non-interpenetrated form crystallises depends on the modulating agent used in our syntheses. Use of benzoic acid gives NU-1200 whereas in the presence of formic acid the interpenetrated structure results. It is likely that during

crystallisation the observed presence of benzoate groups bound to the clusters sterically inhibits the growth of a second, interpenetrating, lattice.

Upon removal of solvent from STA-26, there is a shift in the position of one interpenetrating lattice with respect to the other, resulting in a symmetry change from *Im*−3*m* to *Cmcm*, which is reversible upon reimmersion in DMF (the synthesis solvent). The post-synthetic structural changes are observed not only by X-ray diffraction, but also, remarkably, by solid-state ^{13}C NMR, which shows peak splittings as the symmetry changes. Heating at 125 °C and above results in dehydroxylation of the cluster and IR spectroscopy using Lewis basic probe molecules reveals the presence of Lewis acid sites, likely to be coordinatively unsaturated Zr^{4+} cations.

Activated samples of STA-26 give N_2 adsorption 77 K isotherms of Type I, confirming the microporous nature of the STA-26 structure, compared to the Type IV isotherm of the mesoporous non-interpenetrated analogue NU-1200. CO_2 adsorption shows gradual pore filling at 196 K up to ca. 0.2 bar, which is well described by grand canonical Monte Carlo simulations of adsorption on the microporous interpenetrated structure. While the microporosity and especially the reduced window size of ca. 5 Å will make STA-26 unfavourable for the adsorption and catalytic transformations of large molecules, it possesses good porosity for N_2 and CO_2 even after direct activation from water, demonstrating that it is a stable and size-selective adsorbent.

Experimental Section

Materials and Methods The synthesis of **TMTB**, 4,4',4''-(2,4,6-trimethylbenzene-1,3,5-triyl)tribenzoic acid, was performed by modifying previously reported methods.[8,9,32] A detailed experimental procedure is provided in the Supporting Information. **NU-1200(Zr)** was synthesised by modifying the published work by Liu *et al*.[8] $ZrCl_4$ (48 mg, 0.20 mmol), TMTB (40 mg, 0.08 mmol) and benzoic acid/2-fluorobenzoic acid (1.40/1.61 g, 11.5 mmol) were ultrasonically dissolved in DMF (8 mL) in a pyrex vial. The solution was heated at 120 °C for 48 h in an oven before being cooled to room temperature. The supernatant solution was extracted with a syringe and the resulting white solid was washed multiple times with DMF followed by acetone and dried in an oven at 80 °C (26.0 mg). Single crystals of **STA-26(Zr)** were prepared using a reaction procedure similar to that of Wang *et al* for the synthesis of BUT-12.[9] $ZrCl_4$ (48 mg, 0.20 mmol) and TMTB (40 mg, 0.08 mmol) were ultrasonically dissolved in a solvent mixture of DMF (8 mL) and formic acid (8 mL) in a 20 mL Pyrex vial. The resulting solution was gradually heated to 120 °C with a ramp rate of 3 °C min^{-1} and kept there for 48 h before being cooled to room temperature. The supernatant solution was removed and the colourless crystals obtained were washed multiple times with DMF followed by acetone, then dried in an oven at 80 °C (35.9 mg).

For the synthesis of single phase **STA-26(Zr),** $ZrCl_4$ (48 mg, 0.2 mmol) and TMTB (40 mg, 0.08 mmol) were ultrasonically dissolved in a solvent mixture of DMF (10 mL) and formic acid (6 mL) in a 20 mL Pyrex vial. The resulting solution was gradually heated to 120 °C with a ramp rate of 3 °C min^{-1} and kept there for 48 h before being cooled to room temperature. The supernatant solution was removed and the resulting white solid was washed multiple times DMF followed by acetone, then dried in an oven at 80 °C (53.0 mg). The related **STA-26(Hf)** was synthesised using $HfCl_4$ (64.1 mg, 0.20 mmol) and TMTB (40 mg,

0.08 mmol), ultrasonically dissolved in a solvent mixture of DMF (10 mL) and formic acid (6 mL) in a Pyrex vial. The resulting solution was gradually heated to 120 °C with a ramp rate of 3 °C min^{-1} and kept there for 48 h before being cooled to room temperature. The supernatant solution was removed and the white solid product was washed multiple times with DMF followed by acetone and dried in an oven at 80 °C (55.3 mg).

Materials and methods Powder X-ray diffraction (PXRD) patterns of finely ground powder were collected in Debye-Scherrer geometry from Stoe STAD i/p diffractometers with primary monochromation (Cu $K_{\alpha 1,}$ λ = 1.54056 Å), using 0.7 mm glass capillaries. Variable temperature PXRD (VT-PXRD) measurements were performed in air, with a ramp rate of 5 °C min^{-1} and held at the desired temperature for 10 min prior to measurements. Data were collected from 25 to 200 °C and after cooling down to 25 °C for STA-26(Zr) and STA-26(Zr)-*C*, using a Cobra Plus non-liquid-nitrogen cryostream (Oxford Cryosystems).

For solution-state nuclear magnetic resonance (NMR) spectra of the MOF samples, the protocol developed by Lin *et. al*[33] was used. Prior to analysis, 10 mg of MOF in DMSO-d_6 (0.5 mL) was added to a saturated solution of K_3PO_4 in D_2O (0.5 mL) and stirred at room temperature until the MOF was completely dissolved.

Solid-state NMR spectra were recorded using a Bruker Avance III spectrometer equipped with a 9.4 T superconducting magnet (Larmor frequencies of 400.1 MHz for ^1H and 100.6 MHz for ^{13}C). For the ^{13}C NMR spectra, samples were packed into standard ZrO_2 rotors with an outer diameter of 4 mm and rotated at the magic angle at a rate of 12.5 kHz. Spectra were recorded with cross polarisation (CP) from ^1H with a contact pulse (ramped for ^1H) of 2 ms. Signal averaging was carried out for between 1024 and 19968 transients with a recycle interval of 3 s. Two-pulse phase modulation (TPPM) decoupling of ^1H ($\nu_1 \approx 100$ kHz) was

carried out during acquisition. For the ^{1}H NMR spectra, samples were packed into standard ZrO_2 rotors with an outer diameter of 1.9 mm and rotated at the magic angle at a rate of 40 kHz. Spectra were recorded using a rotor-synchronised spin-echo pulse sequence with an echo delay of 25 μs. Signal averaging was carried out for 64 or 128 transients with a recycle interval of 3 s. Chemical shifts are reported in ppm relative to TMS, using L-alanine as a secondary solid reference ($\mathbf{C}H_3$ δ = 20.5 ppm and $N\mathbf{H}_3$ δ = 8.5 ppm).

Thermogravimetric analysis (TGA) of all samples were carried out on a Netzsch TGA 760 for a temperature range of 20 - 900 °C at a heating rate of 5 °C min^{-1} in a continuous air flow. N_2 adsorption isotherms for STA-26(Zr) and NU-1200 samples were measured volumetrically on a Micrometrics Tristar. The CO_2 adsorptions isotherms were measured gravimetrically on Hiden IGA porosimeter. All samples were activated at 150 °C for 16 h prior to measurements unless otherwise stated.

The IR spectra of STA-26(Zr) on KBr pellet were recorded using a Nicolet Avatar 360 spectrometer (DTGS detector) and the spectra of a self-supporting STA-26(Zr) pellet were recorded using a Nicolet 6700 FTIR spectrometer (MCT detector). During the experiments, up to 128 scans were accumulated at a spectral resolution of 2 cm^{-1} with an accuracy of 0.01 m^{-1}. Specially designed IR cells were used for the experiments. One cell, equipped with CaF_2 windows, permitted the measurement of spectra at low (100 K) and ambient temperatures. Another, equipped with KBr windows, allowed the measurement of spectra at a pre-set temperature in the range between 100 and 300 K. The cells were directly connected to a vacuum-adsorption apparatus with a residual pressure lower than 10^{-3} Pa.

For catalytic studies, both NU-1200 and STA-26(Zr) were activated at 150 °C for 16 h under vacuum. In the test imine formation, 4'-fluoroacetophenone (1 mmol) and benzylamine (1 mmol) in dry, degassed toluene (5 mL) were added to the activated MOF (2 mol%, 42 mg)

and heated with stirring at 90 °C for 24 h under argon. After completion of the reaction, the conversion rates were determined by ^{19}F NMR.

Crystal Structure determination

Single crystal X-ray diffraction (SCXRD) data for body centred STA-26(Zr), here STA-26(Zr)-*I,* and STA-26(Zr)-*C* were collected at 173 K using a Rigaku MM-007HF High brilliance RA generator/confocal optics and Rigaku XtaLAB P100 system, with Cu K_α radiation (λ = 1.54187 Å). Intensity data for all compounds were collected using both ω and ϕ steps, accumulating area detector images spanning at least a hemisphere of reciprocal space. All data were corrected for Lorentz polarization effects. A multiscan absorption correction was applied by using CrysAlisPro.[34] Structures were solved by dual-space methods (SHELXT)[35] and refined by full-matrix least-squares against F^2 (SHELXL-2016/6).[36] Non-hydrogen atoms were refined anisotropically, and alkyl and aryl hydrogen atoms were refined using a riding model. Water hydrogens in STA-26(Zr) were located from the difference map and refined subject to distance and angle restraints. Similar water hydrogens could not be located for STA-26(Zr)-*C*. All calculations were performed using the CrystalStructure interface.[37] The data for STA-26(Zr)-*C* showed non-merohedral twinning (twin law - 0.503 - 0.5 1.014 - 0.487 - 0.5 - 1.014 0.487 - 0.5 0.014, twin fraction 15.5 %), which was accounted for in the refinement, and also showed signs that several further minor twins might also be present; although attempts to refine the data taking these into account did not improve structure quality. Both structures showed large voids, 12119 Å^3 for STA-26(Zr)-*I* (54.2 % of unit cell volume) and 25893 Å^3 for STA-26(Zr)-*C* (57.6 % of unit cell volume) and the SQUEEZE[38] routine implemented in PLATON[39] was used to remove the contribution of the disordered electron density in the void spaces. The crystallographic data (excluding structure factors) of the structures reported in this paper have been deposited into

the Cambridge Crystallographic Data Centre with CCDC Numbers 1571655 for STA-26(Zr)-I and 1571656 for STA-26(Zr)-*C*.

Simulation details

Gas adsorption was simulated using grand canonical Monte Carlo (GCMC) simulations, implemented in the multipurpose code MuSiC.[40] Framework structures were taken from measured or reported crystallographic cif files. The structures were assumed to have dehydrated Zr_6O_8 cores. In addition, disordered H-atoms on the CH_3 groups were ordered for the initial optimisation of the structures. This lowered the symmetry of STA-26(Zr) from *Im*-3*m* to *I*432 and STA-26(Zr)-*C* from *Cmcm* to *C*222. Due to the μVT ensemble imposed in GCMC the framework atoms were fixed in the optimised positions. For each gas (CO_2 and N_2) at each pressure, $1x10^9$ Monte Carlo steps were performed where each step consists of either a random translation, insertion or deletion, and random rotation – all equally weighted. The first 40 % of the steps were used for equilibration and the remaining used to calculate the ensemble averages. Standard Lennard-Jones (LJ) potentials were used to model the dispersive interactions between the framework and gases. The Trappe force field was used to model CO_2, and N_2.[41] Coulombic interactions were included and calculated using Wolf Coulombic summations which are much more efficient than Ewald summations.[42] Interactions beyond 18 Å were neglected. To calculate the gas-phase fugacity the Peng–Robinson equation of state was used.[43]

Acknowledgements We acknowledge the support of the EPSRC/St Andrews Criticat CDT (RRRP, PAW) and the European Community Seventh Framework Program (FP7/2007-2013) number 608490] (project M_4CO_2) (KKC, MYM, KIH, PAW). SEA would like to thank

the Royal Society and Wolfson Foundation for a merit award. This research made use of the Balena High Performance Computing (HPC) Service at the University of Bath. The research data (and/or materials) supporting this publication can be accessed at DOI: XXX.

Electronic Supplementary Information

Supporting information is available on additional NMR and IR spectra, PXRD, electron and optical micrographs, and measured and calculated adsorption isotherms .

References

1. (a) H. Furukawa, K. E. Cordova, M. O'Keeffe, O. M. Yaghi, *Science* **2013**, *341*, 1230444; (b) H.-C. Zhou, J. R. Long, O. M. Yaghi, *Chem. Rev.* **2012**, *112*, 673–674.

(2) (a) K. Sumida, D. L. Rogow, J. A. Mason, T. M. McDonald, E. D. Bloch, Z. R. Herm, T. H. Bae, J. R. Long, *Chem. Rev.* **2012**, *112*, 724–781. (b) J. Li, R. Kuppler, H. Zhou, *Chem. Soc. Rev.* **2009**, *38*, 1477–1504.

(3) (a) L. E. Kreno, K. Leong, O. K. Farha, M. Allendorf, R. P. Van Duyne, J. T. Hupp, *Chem. Rev.* **2012**, *112*, 1105–1125. (b) M. G. Campbell, S. F. Liu, T. M. Swager, M. Dincă, *J. Am. Chem. Soc.* **2015**, *137,* 13780–13783.

(4) (a) J. Liu, L. Chen, H. Cui, J. Zhang, L. Zhang, C.-Y. Su, *Chem. Soc. Rev.* **2014**, *43*, 6011–6061. (b) L. Ma, C. Abney, W. Lin, *Chem. Soc. Rev.* **2009**, *38*, 1248–1256. (c) J. Jiang, O. M. Yaghi, *Chem. Rev.* **2015**, *115*, 6966–6997. (c) M. Rimoldi, A. J. Howarth, M. R. DeStefano, S. Goswami, P. Li, J. T. Hupp, O. K. Farha, *ACS Catal.* **2017**, *7*, 997-1014.

(5) P. Horcajada, R. Gref, T. Baati, P. K. Allan, G. Maurin, P. Couvreur, G. Ferey, R. E. Morris, C. Serre, *Chem. Rev.* **2012**, *112*, 1232-1268.

(6) (a) J. H. Cavka, S. Jakobsen, U. Olsbye, N. Guillou, C. Lamberti, S. Bordiga, K. P. Lillerud, *J. Am. Chem. Soc.* **2008**, *6*, 13850–13851. (b) D. Feng, K. Wang, J. Su, T. F. Liu, J.

Park, Z. Wei, M. Bosch, A. Yakovenko, X. Zou, H. C. Zhou, *Angew. Chem., Int. Ed.* **2015**, *54*, 149–154. (c) V. Bon, I. Senkovska, I. A. Baburin, S. Kaskel, *Cryst. Growth Des.* **2013**, *13*, 1231-1237.

(7) Y. Bai, Y. Dou, L.-H. Xie, W. Rutledge, J.-R. Li, H.-C. Zhou, *Chem. Soc. Rev.* **2016**, *45*, 2327–2367.

(8) T. F. Liu, N. A. Vermeulen, A. J. Howarth, P. Li, A. A. Sarjeant, J. T. Hupp, O. K. Farha, *Eur. J. Inorg. Chem.* **2016**, *27*, 4266.

(9) B. Wang, X. L. Lv, D. Feng, L. H. Xie, J. Zhang, M. Li, Y. Xie, J. R. Li, H. C. Zhou, *J. Am. Chem. Soc.* **2016**, *138*, 6204–6216.

(10) N. Planas, J. E. Mondloch, S. Tussupbayev, J. Borycz, L. Gagliardi, J. T. Hupp, O. K. Farha, C. J. Cramer, *J. Phys. Chem. Lett.* **2014**, *5*, 3716-3723.

(11) D. Yang, V. Bernales, T. Islamoglu, O. K. Farha, J. T. Hupp, C. J. Cramer, L. Gagliardi, B. C. Gates, *J. Am. Chem. Soc.* **2016**, *138*, 15189–15196.

(12) (a) A. Umemura, S. Diring, S. Furukawa, H. Uehara, T. Tsuruoka, S. Kitagawa, *J. Am. Chem. Soc.* **2011**, *133*, 15506–15513. (b) S. Diring, S. Furukawa, Y. Takashima, T. Tsuruoka, S. Kitagawa, *Chem. Mater.* **2010**, *22*, 4531–4538. (c) G. C. Shearer, S. Chavan, S. Bordiga, S. Svelle, U. Olsbye, K. P. Lillerud, *Chem. Mater.* **2016**, *28*, 3749–3761. (d) G. C. Shearer, J. G. Vitillo, S. Bordiga, S. Svelle, U. Olsbye, K. P. Lillerud, *Chem. Mater.* **2016**, *28*, 7190–7193. (e) V. Bon, I. Senkovska, M. S. Weiss, S. Kaskel, *CrystEngComm*, 2013, 15, 9572-9577.

(13) (a) O. K. Farha, C. D. Malliakas, M. G. Kanatzidis, J. T. Hupp, *J. Am. Chem. Soc.* **2010**, *132,* 950-952. (b) A. Schaate, P. Roy, T. Preuße, S. J. Lohmeier, A. Godt, P. Behrens, *Chem. - A Eur. J.* **2011**, *17*, 9320–9325.

(14) J. Lippke, B. Brosent, T. Von Zons, E. Virmani, S. Lilienthal, T. Preuße, M. Hulsmann, A. M. Schneider, S. Wuttke, P. Behrens, A. Godt, *Inorg. Chem.* **2017**, *56*, 748–761.

(15) M. Dincă, A. Dailly, C. Tsay, J. R. Long, *Inorg. Chem.* **2008**, *47*, 11–13.

(16) S. B. Choi, H. Furukawa, H. J. Nam, D. Y. Jung, Y. H. Jhon, A. Walton, D. Book, M. O'Keeffe, O. M Yaghi, J. Kim, *Angew. Chem., Int. Ed.* **2012**, *51*, 8791–8795.

(17) A. Ferguson, L. Liu, S. J. Tapperwijn, D. Perl, F.-X. Coudert, S. Van Cleuvenbergen, T. Verbiest, M. A. van der Veen, S. G. Telfer, *Nat. Chem.* **2016**, *8*, 250–257.

(18) H.-L. Jiang, T. A. Makal, H.-C. Zhou, *Coordination Chemistry Reviews*. **2013**, *257*, 2232-2249.

(19) (a) V. Bon, I. Senkovska, I. A. Baburin, S. Kaskel, *Cryst. Growth Des*. **2013**, 13, 1231-1237. (b) D. Feng, H. -L. Jong, Y. -P. Chen, Z. -Y. Gu, Z. Wei, H. -C. Zhou, *Inorg. Chem*. **2013**, 52, 12661-12667. (c) M. H. Beyzavi, R. C. Klet, S. Tussupbayev, J. Borycz, N. A. Vermeulen, C. J. Cramer, J. F. Stoddart, J. T. Hupp, O. K. Farha, *J. Am. Chem. Soc*. **2014**, *136*, 15861-15864. (d) M. Rimoldi, A. J. Howarth, M. R. DeStefano, L. Lin, S. Goswami, P. Li, J. T. Hupp, O. K. Farha, *ACS Catal*, **2017**, 7, 997-1014.

(20) D. H. Ripin and D. E. Evans, *pKa's of Inorganic and Oxo-Acids*. http:// evans.harvard.edu/pdf/evans_pKa_table.pdf.

(21) L. Valenzano, B. Civalleri, S. Chavan, S. Bordiga, M. H. Nilsen, S. Jakobsen, K. P. Lillerud, C. Lamberti, *Chem. Mater*. **2011**, *23*, 1700–1718.

(22) A. D. Wiersum, E. Soubeyrand-Lenoir, Q. Yang, B. Moulin, V. Guillerm, M. B. Yahia, S. Bourrelly, A. Vimont, S. Miller, C. Vagner, M. Daturi, G. Clet, C. Serre, G. Maurin, P. L. Llewellyn, *Chem. Asian J*. **2011**, *6*, 3270–3280.

(23) N. Planas, J. E. Mondloch, S. Tussupbayev, J. Borycz, L. Gagliardi, J. T. Hupp, O. K. Farha, C. J. Cramer, *J. Phys. Chem. Lett*. **2014**, *5*, 3716–3723.

(24) K. Hadjiivanov, *Adv. Catal*., **2014**, *57*, 99–318.

(25) M. Mihaylov, S. Andonova, K. Chakarova, A. Vimont, E. Ivanova, N. Drenchev, K. Hadjiivanov, *Phys. Chem. Chem. Phys*., **2015**, *17*, 24304–24314.

(26) A. Vimont, H. Leclerc, F. Mauge, M. Daturi, J.-C. Lavalley, S. Surble, C. Serre, G. Férey, *J. Phys. Chem. C*. **2007**, *111*, 383–388.

(27) L. Ma, M. J. Falkowski, C. Abney, W. Lin, *Nat. Chem*. **2010**, *2*, 838-846.

(28) A. J. Howarth, Y. Liu, P. Li, Z. Li, T. C. Wang, J. T. Hupp, O. K. Farha, *Nat. Rev. Mater*. **2016**, *53*, 15018, 15018.

(29) J. E. Mondloch, M. J. Katz, N. Planas, D. Semrouni, L. Gagliardi, J. T. Hupp, O. K. Farha, *Chem. Commun.* **2014**, *50*, 8944–8946.

(30) A. P. Nelson, O. K. Farha, K. L. Mulfort, J. T. Hupp, *J. Am. Chem. Soc.* **2009**, *131*, 458-460.

(31) A. J. Howarth, A. W. Peters, N. A. Vermeulen, T. C. Wang, J. T. Hupp, O. K. Farha, *Chem. Mater.* **2017**, *29*, 26–39.

(32) F. Carson, E. Martínez-Castro, R. Marcos, G. G. Miera, K. Jansson, X. Zou, B. Martín-Matute, *Chem. Commun.* **2015**, *51*, 10864–10867.

(33) N. C. Thacker, Z. Lin, T. Zhang, J. C. Gilhula, C. W. Abney, W. Lin, *J. Am. Chem. Soc.* **2016**, *138*, 3501–3509.

(34) *CrysAlisPro* v1.171.38.43i. Rigaku Oxford Diffraction, Rigaku Corporation, Oxford, U.K. 2015.

(35) G. M. Sheldrick, Crystal structure refinement with SHELXL. *Acta Crystallogr. Sect. A.* **2015**, *71*, 3-8

(36) G. M. Sheldrick, Crystal structure refinement with SHELXL. *Acta Crystallogr. Sect. C.* **2015**, *71*, 3-8.

(37) *CrystalStructure* v4.2. Rigaku Americas, The Woodlands, Texas, USA, and Rigaku Corporation, Tokyo, Japan, 2013.

(38) A. L. Spek, *Acta Crystallogr. Sect C.* **2015**, *71*, 9-18.

(39) A. L. Spek, *Acta Crystallogr. Sect D.* **2009**, *65*, 148-155.

(40) A. Gupta, S. Chempath, M. J. Sanborn, L. A. Clark, R. Q. Snurr, *Mol. Simul.*, **2003**, *29*, 29-46.

(41) J. J. Potoff, J. I. Siepmann, *AIChE J*, **2001**, *47*, 1676-1682.

(42) D. Wolf, P. Keblinski, S. R. Phillpot, J. Eggebrecht, *J. Chem. Phys.*, **1999**, *110*, 8254-8282.

(43) D. Peng, D. B. Robinson, *Ind Eng Chem Fund*, **1976**, *15*, 59-64.

Graphical Abstract